Enhanced Spin-Orbit-Torque Efficiency in W-Co$_{20}$Fe$_{60}$B$_{20}$ Multilayers by Insertion of an Ir$_x$Mn$_{1-x}$ or Pt$_x$Mn$_{1-x}$ Layer

Qingtao Xia,[1,2] Junda Qu,[1,2] Tianren Luo,[1,2] Dandan Zhang,[1,2] Jin Cui,[1] Houyi Cheng,[1,3] Kewen Shi,[1]
Huaiwen Yang,[1,2] Xueying Zhang ®,[1,2] Qiang Li,[4] Sylvain Eimer,[1,3,*] Cong Wang,[1,†]
Dapeng Zhu ®,[1,2,‡] and Weisheng Zhao[1,2,3]

[1]*Fert Beijing Institute, MIIT Key Laboratory of Spintronics, School of Integrated Circuit Science and Engineering, Beihang University, Beijing 100191, China*

[2]*Beihang-Goertek Joint Microelectronics Institute, Qingdao Research Institute, Beihang University, Qingdao 266000, China*

[3]*Hefei Innovation Research Institute, Beihang University, Hefei 230013, China*

[4]*College of Physics, University-Industry Joint Center for Ocean Observation and Broadband Communication, Qingdao University, Qingdao 266071, China*

Spin-orbit torque (SOT) has great potential application for developing next-generation magnetic random-access memory (MRAM). For efficient utilization of the SOT MRAM, most efforts have been focused on reducing power consumption by improving the SOT efficiency. Here, we report that inserting an ultrathin Ir$_x$Mn$_{1-x}$ (or Pt$_x$Mn$_{1-x}$) layer at the heavy-metal–ferromagnet interface is an effective strategy to increase the SOT efficiency. By performing spin-torque ferromagnetic magnetic resonance and second-harmonic Hall measurements, we found that the absolute values of the charge-to-spin conversion efficiency increase from 0.09 for annealed W-Co$_{20}$Fe$_{60}$B$_{20}$ (CFB) sample to 0.15 for annealed W-Ir$_x$Mn$_{1-x}$-CFB sample. The enhancement of the SOT efficiency can be attributed to the reduction of interfacial spin-memory loss at the annealed W-Ir$_x$Mn$_{1-x}$ (or Pt$_x$Mn$_{1-x}$)-CFB samples. Moreover, current-driven magnetization switching with a reduced critical current density has been achieved in the annealed W-Ir$_x$Mn$_{1-x}$-CFB samples. This study highlights the significant roles of the Ir$_x$Mn$_{1-x}$ (or Pt$_x$Mn$_{1-x}$) insertion layer on improving the SOT efficiency and provides a strategy to improve the SOT efficiency through nanoengineering of the Ir$_x$Mn$_{1-x}$ (or Pt$_x$Mn$_{1-x}$) insertion layer for energy-efficient SOT devices.

I. INTRODUCTION

Current-induced spin-orbit torque (SOT) in heavy-metal (HM)–ferromagnet (FM) systems has attracted extensive attention for next-generation magnetic random-access memory (MRAM) because of their high speeds and low power consumption [1,2]. Unlike spin-transfer-torque MRAM, SOT MRAM allows reading and writing current paths to be separated at three-terminal devices [3,4], with the advantages of improved writing speed, endurance, and energy efficiency. For efficient utilization of the HM/FM structures in SOT-induced devices, intense efforts have been focused on enhancing the SOT efficiency [5–9]. In particular, previous studies showed that interfacial effects strongly affected spin-current injection into the FM layer,

such as spin-memory loss (SML) and spin backflow [5,10–13]. For example, researchers have recognized that SML at the HM-FM interfaces could reduce the interfacial spin transparency, which may decrease the SOT efficiency [5,14].

Lately, various studies showed that inserting ultrathin layers into the HM/FM structures could optimize the interface and thus improve the SOT efficiency. The ultrathin layers inserted at the HM-FM interface can be classified as ultrathin nonmagnetic metal (NM) or antiferromagnet (AFM) layers, e.g., Ta/Ir/CFB, W/Ti/CFB, and Pt/NiO/CFB [15–23]. In addition, many efforts have been directed towards improving the effective spin-mixing conductance to enhance the SOT efficiency by inserting ultrathin layers at the HM-FM interface [10,18]. Therefore, high-efficiency and low-power-consumption SOT MRAM devices can be achieved by carefully engineering the interface of the HM/FM structures. For practical applications of SOT MRAM, Ir$_x$Mn$_{1-x}$ (or Pt$_x$Mn$_{1-x}$) has been widely used in the MRAM

---

*sylvaineimer@buaa.edu.cn
†congwang@buaa.edu.cn
‡zhudp@buaa.edu.cn

industries as a key material [24]. Moreover, the HM/CFB/MgO multilayer has been widely adopted owing to its compatibility with the state-of-the-art tunnel magnetoresistance ratio in the CFB/MgO/CFB structure [25]. Heat treatment is generally also required to be compatible with back-end-of-the-line processes of advanced CMOS technologies [26,27]. Therefore, a study of the SOT efficiency of heat-treated HM/CFB/MgO structures upon Ir_xMn_{1-x} (or Pt_xMn_{1-x}) insertion is essential.

Here, we study the SOT efficiency in annealed W-(Ir_xMn_{1-x} or Pt_xMn_{1-x})-$Co_{20}Fe_{60}B_{20}$/MgO multilayers by spin-torque ferromagnetic magnetic resonance (ST FMR) and the second harmonic Hall technique. Compared with the annealed W-CFB sample, the results show that the charge-to-spin conversion efficiency increased by approximately 66% and 20% for the annealed W-Ir_xMn_{1-x}-CFB and W-Pt_xMn_{1-x}-CFB samples respectively. Moreover, the current driven magnetization switching was characterized using a reliable and all-electrical strategy, and a reduced critical current density was achieved in the annealed W-Ir_xMn_{1-x}-CFB sample. We propose that the improvement of the SOT efficiency is due to the reduction of interfacial SML at the annealed W-Ir_xMn_{1-x} (or Pt_xMn_{1-x})-CFB samples. This study demonstrates that annealed W-Ir_xMn_{1-x} (or Pt_xMn_{1-x})-CFB multilayers are promising candidates for the low-power consumption of SOT-induced spintronic devices.

II. EXPERIMENTAL DETAILS

A. Sample fabrication and photolithography

All film stacks studied here were grown using dc and rf magnetron sputtering with a base pressure of about 2×10^{-8} Torr. The MgO layer was deposited using the rf power supply for 80 W, and other metallic materials were deposited using a dc power supply for 50 W at an Ar pressure of about 6 mTorr. Film stacks of W(3.5)/AFM(0.5)/$Co_{20}Fe_{60}B_{20}$(2)/MgO(1.5)/Ta(1.5) (nanometers thick) were deposited on thermally oxidized Si substrates at room temperature. The alloy targets of the AFM layers were $Ir_{20}Mn_{80}$ and $Pt_{80}Mn_{20}$. All samples were capped with a Ta(1.5 nm) layer to prevent the oxidation of the multilayers. To investigate the phase structures of the W layer, high-resolution x-ray diffraction (XRD) was performed for the W films. However, it was found to be difficult to detect the crystal phase for the W layer at thickness of a 3.5 nm. Then we prepared a 10-nm W layer under the same sputtering conditions (power $P = 50$ W) for crystal-phase measurements. The rates were about 0.05 nm/s. After deposition, the samples were annealed under vacuum ($<10^{-6}$ Torr) at 250 °C for 1 h without a magnetic field. The films were then patterned to standard Hall bars (20×120 μm²) and ST-FMR devices (20×60 μm²) through photolithography and dry-etching processes.

B. Magnetic and electrical property measurements

The anomalous Hall effect (AHE) and magnetic hysteresis (M-H) loop of different samples were measured using a Quantum Design physical property measurement system magnetometer for out-of-plane and in-plane applied magnetic fields. ST FMR was measured using a microwave-frequency current, I_{rf}, with a power of 13 dBm and lock-in detection. The in-plane magnetic field was swept at a fixed angle, θ_H, of 45° with respect to the I_{rf}. By changing the channel width and the gap between the ground (G) and signal (S) electrodes, the impedance of the ST-FMR device was adjusted to approximately 50 Ω. For second-harmonic Hall measurements, an ac current with a frequency of 133.3 Hz was injected into the channel of the Hall bar structures. Here, two lock-in amplifiers were used to measure the first- and second-harmonic Hall voltages. Meanwhile, an in-plane magnetic field, H_{ext}, with a constant amplitude was applied. In particular, the direction of H_{ext} was rotated within the x-y plane. Anisotropic magnetoresistance (AMR) and current-induced SOT switching were measured using a custom-made magnetoelectrical transport measurement system. A Keithley 6221 current source and a Keithley 2182A nanovoltmeter were used to supply dc currents (I_{read}) and record dc voltages (V_{dc}), respectively. The AMR signals were measured using the four-point-probe method for all samples. Current-induced SOT switching was measured by injecting a 100-μs current pulse into the channel path of the Hall bar without a magnetic field via a Keithley 4200 instrument. After each pulse, a waiting time of 1 s was considered to exclude thermal effects. Subsequently, a small read current, I_{read}, and magnetic field were applied, the Hall voltage, V_{dc}, was detected by a Keithley 2182 A instrument. The longitudinal Hall resistance, $R_{xx} = V/I_{read}$, was used to characterize the magnetization state. All measurements were performed at room temperature.

III. RESULTS AND DISCUSSION

A. In-plane magnetic anisotropy of W/AFM/CFB/MgO

To characterize the magnetic properties of the different multilayers, M-H and AHE measurements were performed at room temperature. Figure 1(a) shows the in-plane M-H loops for all the annealed samples. The amplitude of the saturation magnetization (M_s) was approximately 1300 emu/cm³ for the annealed W-CFB sample. However, M_s decreased in the annealed W-Ir_xMn_{1-x}(Pt_xMn_{1-x})-CFB sample. This phenomenon could be due to Mn diffusing into CFB upon annealing at temperatures above 200 °C [28,29], which could decrease the M_s of CFB in our experiments. Notably, the M_s value of the $Ir_{20}Mn_{80}$-base multilayers is smaller than those of the $Pt_{80}Mn_{20}$-base multilayers owing to the different proportions of Mn.
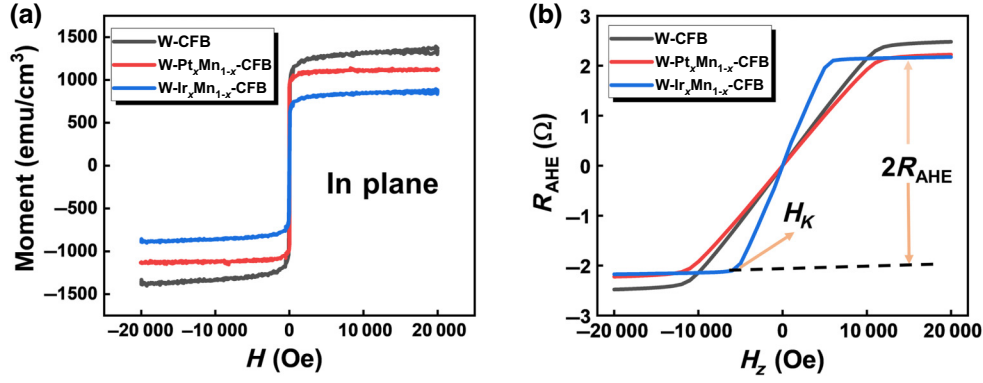
FIG. 1. (a) In-plane hysteresis loops for W-CFB, W-Ir$_x$Mn$_{1-x}$-CFB, and W-Pt$_x$Mn$_{1-x}$-CFB samples annealed at 250 °C. (b) R_{AHE} as a function of out-of-plane magnetic field for W-CFB, W-Ir$_x$Mn$_{1-x}$-CFB, and W-Pt$_x$Mn$_{1-x}$-CFB samples annealed at 250 °C.

The AHE curves of all the samples are presented in Fig. 1(b). Similarly, the amplitude of R_H decreased in the annealed W-Ir$_x$Mn$_{1-x}$ (Pt$_x$Mn$_{1-x}$)-CFB multilayers. The above results show that Co-Fe-B exhibits an in-plane easy axis in all samples. Moreover, we could determine the value of M_s; anomalous Hall resistance coefficient, R_{AHE}; and effective perpendicular anisotropy field, H_K; these are required for the determination of SOT efficiency by ST-FMR and second-harmonic Hall measurements. To investigate the AFM properties of the 0.5-nm-thick Ir$_x$Mn$_{1-x}$ and Pt$_x$Mn$_{1-x}$ layers, M-H loop measurements were performed at different temperatures (see the Supplemental Material [30]). The exchange-bias field (H_{EB}) for W-Pt$_x$Mn$_{1-x}$-CFB is −675 and −75 Oe at 2 and 10 K, respectively. H_{EB} for W-Ir$_x$Mn$_{1-x}$-CFB is −970 and −50 Oe at 2 and 10 K, respectively. These results suggest that the Ir$_x$Mn$_{1-x}$ and Pt$_x$Mn$_{1-x}$ layers, with a thickness of 0.5 nm, exhibit antiferromagnetic properties, holding long-range antiferromagnetic ordering at low temperature. However, H_{EB} for all samples disappears at 300 K, which indicates that the long-range antiferromagnetic ordering also disappears at 300 K.

B. ST-FMR results

All samples were first characterized by ST-FMR measurements to evaluate the SOT efficiency. Figure 2(a) shows a typical ST-FMR device and a schematic diagram of the radio-frequency (rf) circuit for the W/AFM/CFB device. As the radio-frequency charge current was injected into the heavy-metal layer, nonequilibrium spins were generated and flowed to the W-CFB interface owing to the spin Hall effect from the W layer. Subsequently, the spins could be absorbed into the adjacent CFB layer to produce an oscillating dampinglike torque (τ_{DL}) and fieldlike torque (τ_{FL}). These torques, with the Oersted field torque applied to the CFB magnetic moment, caused precession, producing an oscillatory AMR in the ST-FMR device with the same frequency. Consequently, the oscillation of the

AMR and charge current could produce a mixing voltage (V_{mix}), which could be detected by a lock-in amplifier [41,42]. Figure 2(b) shows the ST-FMR spectra of the annealed W-Ir$_x$Mn$_{1-x}$-CFB sample in the frequency range of 5–9 GHz. For all the annealed samples, the full magnetic field ranges of the ST-FMR spectra are shown in the Supplemental Material [30]. To determine the SOT efficiency, we first fit the resonance spectrum with symmetric and antisymmetric Lorentzian contributions using [43]

$$V_{mix} = V_S \frac{\Delta^2}{\Delta^2 + (H_{ext} - H_0)^2} + V_A \frac{\Delta(H_{ext} - H_0)}{\Delta^2 + (H_{ext} - H_0)^2}. \tag{1}$$

Here, V_S and V_A are the symmetric and antisymmetric Lorentzian coefficients, respectively; Δ is the linewidth of the spectra; H_0 is the resonant magnetic field; and H_{ext} is the external magnetic field. The values of V_S, V_A, Δ, and H_0 are obtained by fitting the ST-FMR spectra using Eq. (1). Figure 2(c) shows a typical fitting of the detected ST-FMR signal for the annealed W-Ir$_x$Mn$_{1-x}$-CFB sample at 6 GHz. The symmetric component is attributed to the dampinglike torque, and the antisymmetric component is generated by the total contribution of the fieldlike and Oersted field torques. Notably, the symmetric component, V_S, is larger than the antisymmetric component, V_A, suggesting that a larger τ_{DL} is observed in the annealed W-Ir$_x$Mn$_{1-x}$-CFB sample. Figure 2(d) shows the resonant frequency, f, as a function of the resonant field, H_0, for the annealed W-Ir$_x$Mn$_{1-x}$-CFB sample, which can be fitted using the Kittel formula as follows [44]:

$$f = (\gamma/2\pi)\mu_0 \sqrt{(H_0 + H_\parallel^K)(H_0 + H_\parallel^K + 4\pi M_{eff})}, \tag{2}$$

where γ is the gyromagnetic ratio and $4\pi M_{eff}$ is the effective magnetization of the CFB layer. $H_\parallel^K$ is the in-plane magnetic anisotropy of the CFB layer. $H_\parallel^K$ is measured to be ≤ 12 Oe in all samples from AMR measurements.
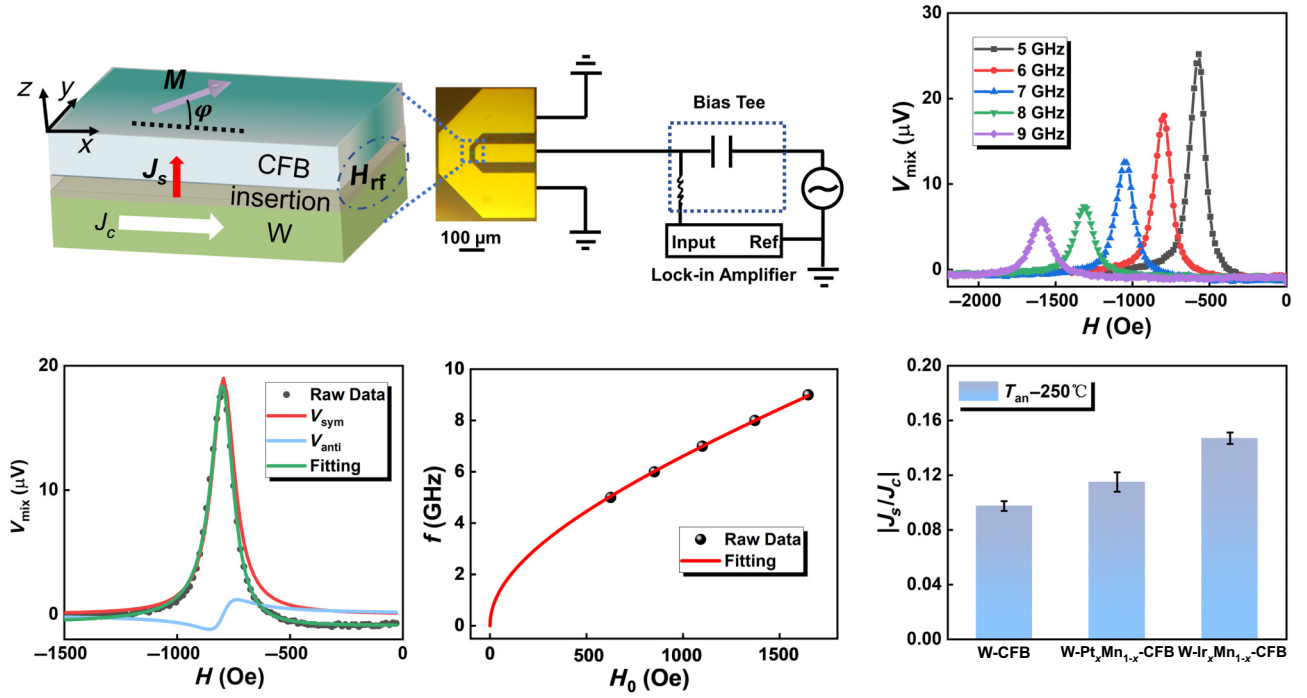
FIG. 2.   (a) Schematic of the ST-FMR measurement setup and illustration of the ST-FMR device with SOT-induced magnetization dynamics. (b) ST-FMR spectra of the W-Ir_xMn_{1-x}-CFB annealed sample in the frequency range of 5–9 GHz (dots). (c) Fitting curve (line) of W-Ir_xMn_{1-x}-CFB device at 6 GHz. (d) Resonant frequency, f, as a function of resonant field, H_0. Solid curve represents a fit to the Kittel formula. (e) SOT efficiency, $|J_s/J_c|$, for all the annealed samples.

The value of $H_\parallel^K$ is 1–2 orders of magnitude smaller than H_0. Therefore, to fit the Kittel formula, the error caused by the contribution of the in-plane magnetic anisotropy field is approximately less than 2%. From the fitting, $4\pi M_{eff}$ can be calculated as 0.48, 0.89, and 1 T for the annealed W-Ir_xMn_{1-x}-CFB, W-Pt_xMn_{1-x}-CFB, and W-CFB samples, respectively. Furthermore, the results from different samples show that the variation trend of $4\pi M_{eff}$ is the same as that of M_s from the M-H loop results. Finally, based on the above results, the ratios of current-to-spin conversion efficiency (i.e., spin Hall angle), defined as $\theta_{CS} = J_s/J_c$, can be calculated using [43]

$$|\theta_{CS}| = \frac{J_s}{J_c} = |\frac{S}{A}| \frac{e\mu_0 M_s td}{\hbar}[1 + 4\pi M_{eff}/H_{ext})]^{1/2}, \quad (3)$$

where t and d are the thicknesses of the CFB and W layers, respectively; e is the charge of the electron; $\hbar$ is the reduced Planck constant; and μ_0 is the vacuum permeability. Figure 2(e) summarizes the calculated J_s/J_c values of the annealed samples. Consequently, J_s/J_c of the annealed W-CFB sample is -0.09 ± 0.007, and J_s/J_c of the annealed W-Pt_xMn_{1-x}-CFB and annealed W-Ir_xMn_{1-x}-CFB samples increases to -0.11 ± 0.01 and -0.15 ± 0.006, respectively. It is well known that the phase structures of W significantly affect the spin-orbit-torque efficiency [31]. To investigate the phase structures of the W layers, XRD

was performed. However, it is difficult to detect the crystal phase of the W layer at a thickness of 3.5 nm (see the Supplemental Material [30]). The 10-nm W layer was also grown at the same sputtering power ($P = 50$ W) for crystal-phase measurements. As a result, it shows only one α-W (110) diffraction peak for the 10-nm W layer. In this study, the crystal phase of the W layer grown with a sputtering power of 50 W is α phase, which is consistent with the findings reported in previous studies [32,33]. In this sense, we speculate that the low spin Hall angle in this work is probably induced by an alpha phase of the W layer deposited with a high sputtering power in experiments. The reason for the enhancement in θ_{CS} by insertion of the AFM layer is discussed in the Sec. III C.

C. Second-harmonic Hall results

The dampinglike torque is the main SOT in the annealed W/AFM/CFB samples from the ST-FMR results; thus, the second-harmonic Hall measurements are exploited to determine the dampinglike torque efficiency, ξ_{DL}, to further confirm the variation in the SOT efficiency. A micrograph of the Hall bar device structure and an illustration of the in-plane second-harmonic Hall measurement setup are shown in Fig. 3(a). When the ac passes through the W layer, the current-induced effective oscillation field can modify the magnetization angle in the CFB layer [34]. Consequently, the first- (R_ω) and second- ($R_{2\omega}$) harmonic
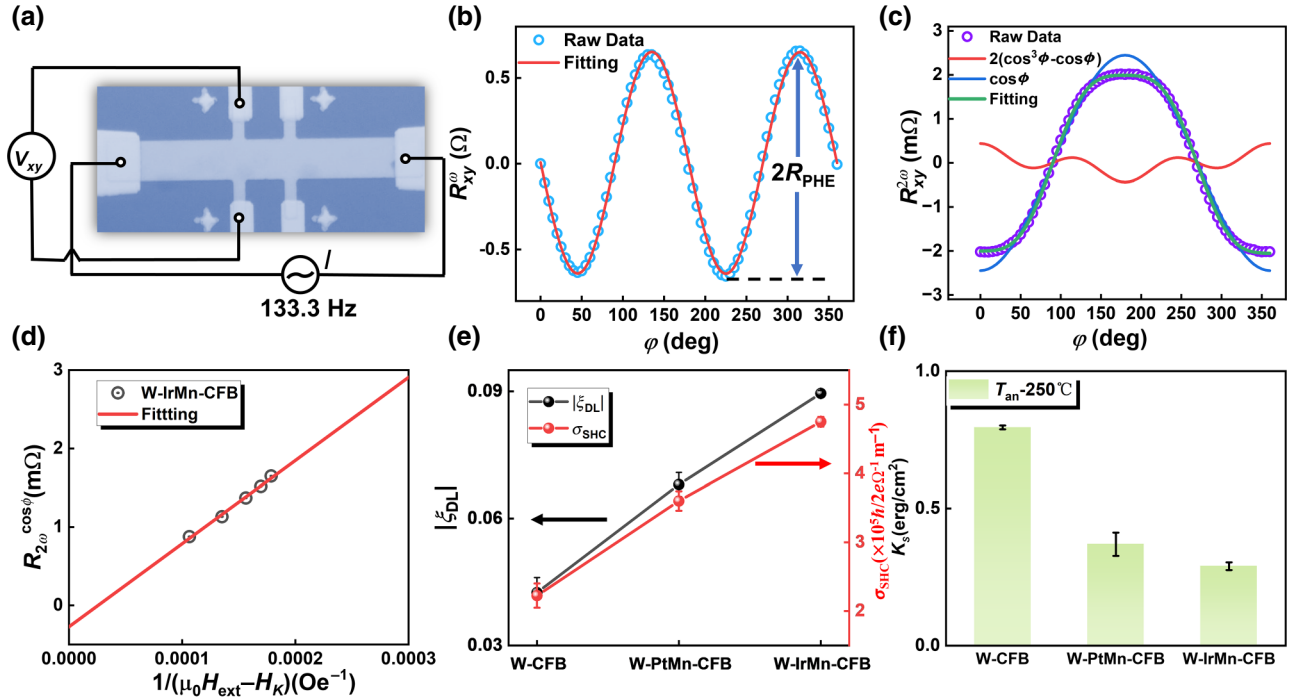
FIG. 3.   (a) Second-harmonic Hall measurements illustrated on the microscope image. (b),(c) First- and second-harmonic Hall resistances as a function of in-plane angle for the W-Ir$_x$Mn$_{1-x}$-CFB sample annealed at 250 °C, under an external magnetic field of 600 Oe. Solid curve represents a fitting curve. (d) $1/(H_{ext}–H_K)$ dependence of the cosφ term of $R_{2\omega}$ for the annealed W-Ir$_x$Mn$_{1-x}$-CFB sample. (e) $|\xi_{DL}|$ and σ_{SHC} and (f) K_s for different samples.

Hall resistances typically contain contributions from both the AHE and the planar Hall effect (PHE). For all the annealed samples, the first- and second-harmonic Hall voltages as a function of the in-plane rotation angle, φ, are shown in the Supplemental Material [30]. Figures 3(b) and 3(c) show R_ω and $R_{2\omega}$ as a function of the in-plane rotation angle, φ, for the annealed W-Ir$_x$Mn$_{1-x}$-CFB sample under an external magnetic field of 600 Oe. As shown in Fig. 3(b), the planar Hall resistance coefficient (R_{PHE}) can be extracted from fitting the $R_\omega - \varphi$ curve as follows [45,46]:

$$R_\omega = R_{PHE} \sin 2\varphi, \tag{4}$$

where $R_{2\omega}$ is dominated by AHE and PHE harmonically, as expressed by [45,46]

$$R_{2\omega} = 2R_{PHE}(2\cos^3\varphi - \cos\varphi)\frac{H_{FL} + H_{Oe}}{H_{ext}}$$
$$- \left(R_{AHE}\frac{H_{DL}}{H_{ext} - H_K} + R_T\right)\cos\varphi, \tag{5}$$

where H_{DL} and H_{FL} are dampinglike (DL) and fieldlike (FL) effective fields, respectively. R_T is the second-harmonic Hall resistance coefficient owing to thermal effects, and H_{Oe} is the Oersted field induced by the current flowing into the W layer. The anomalous Hall resistance coefficient, R_{AHE}, and the effective perpendicular

anisotropy field, H_K, can be obtained from the above results, as shown in Fig. 1(b). Moreover, the H_{ext} dependence of $R_{2\omega}$ was measured to eliminate R_T from the cosφ component to obtain H_{DL}. Figure 3(d) shows $R_{2\omega}^{\cos\varphi}$ as a function of $1/(H_{ext} - H_k)$. From the linear fitting, H_{DL} was calculated to be (4.78 ± 0.31) Oe for the annealed W-Ir$_x$Mn$_{1-x}$-CFB sample. Similarly, H_{DL} was calculated to be (2.78 ± 0.31) Oe for the annealed W-Pt$_x$Mn$_{1-x}$-CFB sample and (2.13 ± 0.11) Oe for the annealed W-CFB sample. Then, a dimensionless dampinglike torque efficiency, ξ_{DL}, could be given by [21]

$$\xi_{DL} = \frac{2eH_{DL}M_s}{\hbar J_c}, \tag{6}$$

where J_c is the current density through W. Figure 3(e) shows the ξ_{DL} value of different samples determined using Eq. (6). The estimated values of ξ_{DL} for the annealed samples were -0.09 ± 0.001 for W-Ir$_x$Mn$_{1-x}$-CFB, -0.07 ± 0.003 for W-Pt$_x$Mn$_{1-x}$-CFB, and -0.04 ± 0.005 for W-CFB. The variation trend of the ξ_{DL} values is similar to the ST-FMR results. However, ξ_{FL} is smaller than ξ_{DL} for all the samples, which indicates that the dampinglike torque is the main SOT in our samples. ξ_{FL} is also discussed for all the samples in the Supplemental Material [30]. Based on the second-harmonic measurements, the spin Hall conductivity (σ_{SHC}), an important

parameter for practical applications, is calculated by [47]

$$\sigma_{SHC} = (\hbar/2e)\xi_{DL}/\rho_W \qquad (7)$$

where ρ_W is the resistivity of the W layer. The values of σ_{SH} are approximately 2.1×10^4, 3.7×10^4, and 4.7×10^4 $\hbar/2e\,\Omega^{-1}\,m^{-1}$ for the annealed W-CFB, W-Pt_xMn_{1-x}-CFB, and W-Ir_xMn_{1-x}-CFB samples, respectively, as shown in Fig. 3(e). The variation trend of σ_{SHC} among different samples is consistent with the SOT efficiency.

For the underlying mechanism for the enhancement of the SOT efficiency, we first exclude the spin-orbit-torque contributions from the Ir_xMn_{1-x} and Pt_xMn_{1-x} insertion layers, because the spin Hall angle has the opposite sign to that of the W layer [2,48]. Second, the enhancement of the SOT efficiency is not related to the antiferromagnetic order of Ir_xMn_{1-x} and Pt_xMn_{1-x}, as no long-range antiferromagnetic order is present at room temperature in these insertion layers. In contrast, as we mentioned above, interfacial effects play an important role in spin transmission at the HM-FM interface. Especially SML, which is the loss of spin information due to spin-flip scattering at the interface, is widely recognized to occur when the spin angular momentum carried by the spin current fails to be transferred to the magnetic layer due to the spin-orbit scattering occurring at the interface of the heavy metal-ferromagnetic metal. Previous work reported that the SML at the HM-FM interfaces could reduce the interfacial spin transparency, which might decrease the SOT efficiency [49]. The interfacial effects on spin transmission could be quantified with the effective spin-mixing conductance, $G_{eff}^{\uparrow\downarrow}$ [35,36]. Both the spin-mixing conductance and the SOT efficiency are enhanced by inserting an AFM layer in our samples (see the Supplemental Material [30]). So, we believe that the metallic AFM insertion layer would optimize the W-CFB interface in our work. Previous studies demonstrated that the HM atoms with a strong spin-orbit coupling (e.g., $5d$ W, Ir, and Pt) could modify the orbital moments of the adjacent FM atoms (e.g., $3d$ Co and Fe) via strong interfacial spin-orbit coupling (ISOC) [50,51]. Recently, Zhu *et al.* demonstrated that the ISOC was the dominant mechanism for SML, which could reduce the SOT efficiency [5,11]. Therefore, in this study, the possible reduced SML was quantified by determining the interfacial magnetic anisotropy energy density (K_s), as an indicator of the strength of ISOC, as follows [11]:

$$4\pi M_{eff} \approx 4\pi M_s - \frac{2K_s}{M_{area}}, \qquad (8)$$

where M_{area} is the in-plane magnetization per unit area for each sample. As shown in Fig. 3(f), we calculated K_s to be (0.79 ± 0.008) erg/cm^2 for annealed W-CFB, (0.37 ± 0.042) erg/cm^2 for annealed W-Pt_xMn_{1-x}-CFB,

and (0.29 ± 0.014) erg/cm^2 for annealed W-Ir_xMn_{1-x}-CFB. As expected, the reduced K_s in annealed W/AFM/CFB suggests degradation of the interfacial SML [4], which would strengthen the SOT efficiency. Furthermore, it is widely recognized that reducing SML would result in a decrease in magnetic damping [9,37]. Based on the ST-FMR results, magnetic damping is studied by the linear fitting of the resonance linewidth, Δ, with respect to frequency, f (see the Supplemental Material [30]). The magnetic damping is 0.0227 ± 0.0007, 0.0157 ± 0.0006, and 0.0163 ± 0.0007 for the annealed W-CFB, W-Pt_xMn_{1-x}-CFB, and W-Ir_xMn_{1-x}-CFB samples, respectively. As expected, by inserting the AFM layer in our samples, the interfacial spin-memory loss is reduced, leading to a decrease in the damping coefficient. We suggest that Mn, a $3d$ element with weaker spin-orbit coupling compared to W, is likely to lead to a reduction of the spin-flip scattering at the interfaces. As a result, SML is reduced at the W-CFB interface by the insertion of Ir_xMn_{1-x} or Pt_xMn_{1-x} at the interface. Consequently, SML at the interface is reduced, leading to a decrease in α and an increase in the SOT efficiency. In this work, H_{EB} for all samples disappears at 300 K, which indicates that long-range antiferromagnetic ordering also disappears at 300 K. Thus, in this work, the enhanced SOT efficiency achieved by inserting the Ir_xMn_{1-x} or Pt_xMn_{1-x} layer at room temperature is not associated with the antiferromagnetic properties. Therefore, this result could explain the enhancement of θ_{CS} and ξ_{DL} in the annealed W/AFM/CFB samples compared with the annealed W-CFB samples.

D. Spin-orbit-torque switching

A reliable and all-electrical strategy was used to probe SOT-induced magnetization switching by analyzing the AMR signal [52,53]. The strategy was implemented to demonstrate that the SOT efficiency enhancement could reduce the critical SOT switching current density. Figures 4(a) and 4(b) illustrate the process diagrams of the magnetization-switching measurements. The pulse current, I_{pulse}, sweeps from negative to positive values and returns to negative values without an external magnetic field. After each pulse current, the read currents, I_{read} (1 mA), and assisting magnetic field, H_{assist} (± 7 or ± 6 Oe), were applied to detect the AMR signals. Figure 4(c) shows R_{xx} as a function of the in-plane magnetic field along the y direction for annealed W-CFB and the origin of these two different resistance states in R_{xx}. R_{xx} of the device can be switched between a high-resistance state and a low-resistance state at a critical switching current density of $J_p \approx 2.4 \times 10^7$ A/cm^2 [Figs. 4(d) and 4(e)]. Notably, the polarities of the current-induced switching loops are opposite when the opposite assisting magnetic field is applied. Similarly, deterministic current-induced magnetization switching can be realized
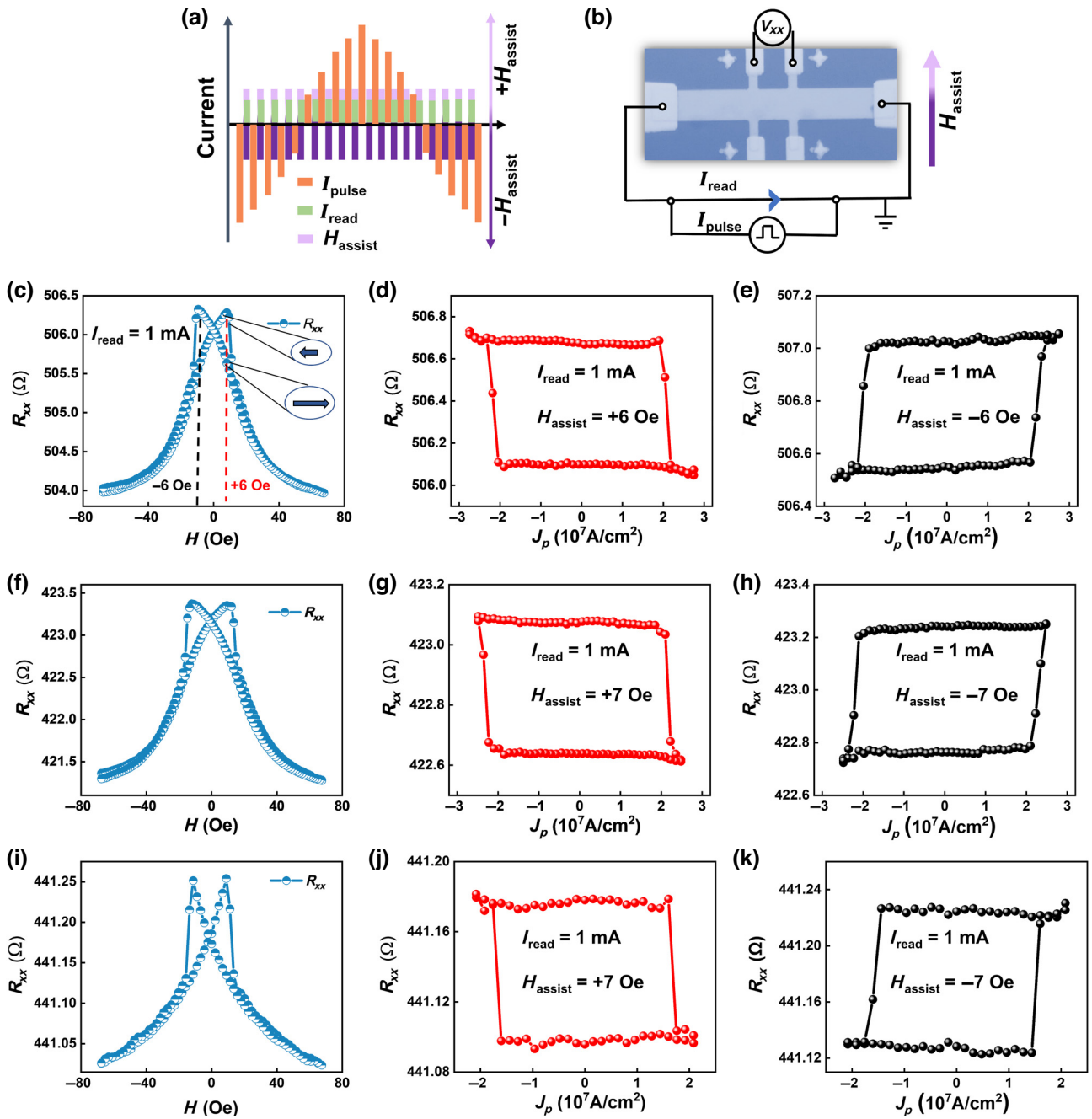
FIG. 4.   (a) Measurement sequence for the switching experiment. (b) Switching and AMR measurements illustrated on a microscope image. (c)–(e) AMR loops obtained for the W-CFB annealed sample and the variation in resistance versus current density with $H_{\text{assist}} = \mp 6$ Oe. (f)–(h) AMR loops obtained for the W-Pt$_x$Mn$_{1-x}$-CFB annealed sample and the variation in resistance versus current density with $H_{\text{assist}} = \mp 7$ Oe. (i)–(k) AMR loops obtained in the W-Ir$_x$Mn$_{1-x}$-CFB annealed sample and the variation in resistance versus current density with $H_{\text{assist}} = \mp 7$ Oe.

in the annealed W-Pt$_x$Mn$_{1-x}$-CFB and W-Ir$_x$Mn$_{1-x}$-CFB samples, as shown in Figs. 4(f)–4(k). As expected, the lowest critical switching current density was approximately 1.5×10^7 A/cm^2 for the annealed W-Ir$_x$Mn$_{1-x}$-CFB sample, which was smaller than that of 2×10^7 A/cm^2 for the annealed W-CFB sample and 2.4×10^7 A/cm^2 for the annealed W-Pt$_x$Mn$_{1-x}$-CFB sample. However, it

is worth noting that the critical current density in the annealed W-Pt$_x$Mn$_{1-x}$-CFB sample is higher than that of the annealed W-CFB sample, which is inconsistent with the results from ST-FMR and second-harmonic Hall measurements. Since the critical current density is proportional to the H_c/ξ_{DL} [47,53], we believe that the extrinsic value of coercivity, H_c, is essential for SOT-induced magnetization

switching, and H_c could be affected by the micrometer size of the devices [54]. As shown in Figs. 4(f) and 4(c), the value of H_c for the annealed W-Pt$_x$Mn$_{1-x}$-CFB sample (12 Oe) is larger than that of the annealed W-CFB sample (9 Oe), producing a slightly larger current density in the annealed W-Pt$_x$Mn$_{1-x}$-CFB sample. Therefore, these results suggest that the annealed W-Ir$_x$Mn$_{1-x}$-CFB sample might be the most optimized sample for SOT-based applications owing to its low critical current density and high SOT efficiency.

IV. CONCLUSION

We studied the SOT efficiency in annealed W-Ir$_x$Mn$_{1-x}$ (or Pt$_x$Mn$_{1-x}$)-CFB samples. Based on ST-FMR and second-harmonic Hall measurements, we showed that the SOT efficiency could be enhanced by inserting an Ir$_x$Mn$_{1-x}$ (or Pt$_x$Mn$_{1-x}$) layer at the W-CFB interface. Moreover, in-plane magnetization switching with a reduced critical current density was achieved in the annealed W-Ir$_x$Mn$_{1-x}$-CFB sample. The enhanced SOT efficiency in annealed W-Ir$_x$Mn$_{1-x}$ (or Pt$_x$Mn$_{1-x}$)-Co-Fe-B could be attributed to the decrease in interfacial spin-memory loss. This study provides a strategy to improve the SOT efficiency through nanoengineering of the Ir$_x$Mn$_{1-x}$ (or Pt$_x$Mn$_{1-x}$) insertion layer for low-power-consumption SOT-induced spintronic devices.

ACKNOWLEDGMENTS

———

[1] R. Ramaswamy, J. M. Lee, K. Cai, and H. Yang, Recent advances in spin-orbit torques: Moving towards device applications, Appl. Phys. Rev. **5,** 031107 (2018).

[2] S. Peng, D. Zhu, W. Li, H. Wu, A. J. Grutter, D. A. Gilbert, J. Lu, D. Xiong, W. Cai, P. Shafer, K. L. Wang, and W. Zhao, Exchange bias switching in an antiferromagnet/ferromagnet bilayer driven by spin–orbit torque, Nat. Electron. **3,** 757 (2020).

[3] V. Krizakova, M. Perumkunnil, S. Couet, P. Gambardella, and K. Garello, Spin-orbit torque switching of magnetic tunnel junctions for memory applications, J. Magn. Magn. Mater. **562,** 169692 (2022).

[4] A. Manchon, J. Železný, I. M. Miron, T. Jungwirth, J. Sinova, A. Thiaville, K. Garello, and P. Gambardella, Current-induced spin-orbit torques in ferromagnetic and antiferromagnetic systems, Rev. Mod. Phys. **91,** 3 (2019).

[5] L. Zhu, D. C. Ralph, and R. A. Buhrman, Spin-orbit torques in heavy-metal-ferromagnet bilayers with varying strengths of interfacial spin-orbit coupling, Phys. Rev. Lett. **122,** 077201 (2019).

[6] L. Zhu, D. C. Ralph, and R. A. Buhrman, Maximizing spin-orbit torque generated by the spin Hall effect of Pt, Appl. Phys. Rev. **8,** 031308 (2021).

[7] L. Zhu, D. C. Ralph, and R. A. Buhrman, Highly efficient spin-current generation by the spin Hall effect in Au$_{1-x}$Pt$_x$, Phys. Rev. Appl. **10,** 031001 (2018).

[8] Z. Xu, G. D. Hwee Wong, J. Tang, E. Liu, W. Gan, F. Xu, and W. S. Lew, Giant spin Hall effect in Cu-Tb alloy thin films, ACS Appl. Mater. Interfaces **12,** 32898 (2020).

[9] L. Zhu, D. C. Ralph, and R. A. Buhrman, Effective spin-mixing conductance of heavy-metal-ferromagnet interfaces, Phys. Rev. Lett. **123,** 057203 (2019).

[10] L. Zhu, L. Zhu, and R. A. Buhrman, Fully spin-transparent magnetic interfaces enabled by the insertion of a thin paramagnetic NiO layer, Phys. Rev. Lett. **126,** 107204 (2021).

[11] L. Zhu, D. C. Ralph, and R. A. Buhrman, Enhancement of spin transparency by interfacial alloying, Phys. Rev. B **99,** 180404(R) (2019).

[12] L. Zhu, K. Sobotkiewich, X. Ma, X. Li, D. C. Ralph, and R. A. Buhrman, Strong damping-like spin-orbit torque and tunable Dzyaloshinskii–Moriya interaction generated by low-resistivity Pd$_{1-x}$Pt$_x$ alloys, Adv. Funct. Mater. **29,** 1805822 (2019).

[13] J. Ryu, S. Lee, K. J. Lee, and B. G. Park, Current-induced spin-orbit torques for spintronic applications, Adv. Mater. **32,** e1907148 (2020).

[14] J. C. Rojas-Sánchez, N. Reyren, P. Laczkowski, W. Savero, J. P. Attané, C. Deranlot, M. Jamet, J. M. George, L. Vila, and H. Jaffrès, Spin pumping and inverse spin Hall effect in platinum: The essential role of spin-memory loss at metallic interfaces, Phys. Rev. Lett. **112,** 106602 (2014).

[15] A. Razavi, H. Wu, Q. Shao, C. Fang, B. Dai, K. Wong, X. Han, G. Yu, and K. L. Wang, Deterministic spin-orbit torque switching by a light-metal insertion, Nano Lett. **20,** 3703 (2020).

[16] D. Xiong, S. Peng, J. Lu, W. Li, H. Wu, Z. Li, H. Cheng, Y. Wang, C. H. Back, K. L. Wang, and W. Zhao, Modulation of thermal stability and spin–orbit torque in IrMn/CoFeB/MgO structures through atom thick W insertion, Appl. Phys. Lett. **117,** 212401 (2020).

[17] R. Q. Zhang, L. Y. Liao, X. Z. Chen, H. Q. Wu, F. Pan, and C. Song, Strong magnetoresistance modulation by Ir insertion in a Ta/Ir/CoFeB trilayer, Phys. Rev. B **100,** 144425 (2019).

[18] H. Wang, J. Finley, P. Zhang, J. Han, J. T. Hou, and L. Liu, Spin-orbit-torque switching mediated by an antiferromagnetic insulator, Phys. Rev. Appl. **11,** 044070 (2019).

[19] Y. Wang, D. Zhu, Y. Yang, K. Lee, R. Mishra, G. Go, S.-H. Oh, D.-H. Kim, K. Cai, E. Liu, S. D. Pollard, S. Shi, J. Lee, K. L. Teo, Y. Wu, K.-J. Lee, and H. Yang, Magnetization switching by magnon-mediated spin torque through an antiferromagnetic insulator, Science **366,** 1125 (2019).

[20] J. Li, C. B. Wilson, R. Cheng, M. Lohmann, M. Kavand, W. Yuan, M. Aldosary, N. Agladze, P. Wei, M. S. Sherwin, and J. Shi, Spin current from sub-terahertz-generated antiferromagnetic magnons, Nature **578,** 70 (2020).

[21] D. Zhu, T. Zhang, X. Fu, R. Hao, A. Hamzić, H. Yang, X. Zhang, H. Zhang, A. Du, D. Xiong, K. Shi, S. Yan, S. Zhang, A. Fert, and W. Zhao, Sign change of spin-orbit torque in Pt/NiO/CoFeB structures, Phys. Rev. Lett. **128,** 217702 (2022).

[22] Z. Z. Zhang, K. L. Lin, Y. Zhang, A. Bournel, K. Xia, M. Klaui, and W. S. Zhao, Magnon scattering modulated by omnidirectional hopfion motion in antiferromagnets for meta-learning, Sci. Adv. **9,** 12 (2023).

[23] H. Wang, C. Du, P. C. Hammel, and F. Yang, Antiferromagnonic spin transport from $Y_3Fe_5O_{12}$ into NiO, Phys. Rev. Lett. **113,** 097202 (2014).

[24] H. Zhang, X. Ma, C. Jiang, J. Yin, S. Lyu, S. Lu, X. Shang, B. Man, C. Zhang, D. Li, S. Li, W. Chen, H. Liu, G. Wang, K. Cao, Z. Wang, and W. Zhao, Integration of high-performance spin-orbit torque MRAM devices by 200-mm-wafer manufacturing platform, J. Semicond. **43,** 102501 (2022).

[25] Q. Pan, Y. Liu, H. Wu, P. Zhang, H. Huang, C. Eckberg, X. Che, Y. Wu, B. Dai, Q. Shao, and K. L. Wang, Efficient spin-orbit torque switching of perpendicular magnetization using topological insulators with high thermal tolerance, Adv. Electron. Mater. **8,** 2200003 (2022).

[26] D. Wu, G. Yu, Q. Shao, X. Li, H. Wu, K. L. Wong, Z. Zhang, X. Han, P. Khalili Amiri, and K. L. Wang, In-plane current-driven spin-orbit torque switching in perpendicularly magnetized films with enhanced thermal tolerance, Appl. Phys. Lett. **108,** 212406 (2016).

[27] K. Yamane, Y. Higo, H. Uchida, Y. Nanba, S. Sasaki, H. Ohmori, K. Bessho, and M. Hosomi, Spin torque switching of perpendicularly magnetized CoFeB-based tunnel junctions with high thermal tolerance, IEEE Trans. Magn. **49,** 4335 (2013).

[28] A. Maesaka, N. Sugawara, A. Okabe, and M. Itabashi, Influence of microstructure on thermal stability of spin-valve multilayers, J. Appl. Phys. **83,** 7628 (1998).

[29] J. Jeong, Y. Ferrante, S. V. Faleev, M. G. Samant, C. Felser, and S. S. P. Parkin, Termination layer compensated tunnelling magnetoresistance in ferrimagnetic Heusler compounds with high perpendicular magnetic anisotropy, Nat. Commun. **7,** 10276 (2016).

[30] See the Supplemental Material http://link.aps.org/supplemental/10.1103/PhysRevApplied.21.014016 for the *M-H* loop and XRD characterization of the samples, raw data for ST-FMR and second-harmonic Hall measurements, FL-SOT efficiency, magnetic damping, and effective spin-mixing conductance for the samples. It also includes Refs. [9,31–40].

[31] C.-F. Pai, L. Liu, Y. Li, H. W. Tseng, D. C. Ralph, and R. A. Buhrman, Spin transfer torque devices utilizing the giant spin Hall effect of tungsten, Appl. Phys. Lett. **101,** 122404 (2012).

[32] Y. Li, X. Zha, Y. Zhao, Q. Lu, B. Li, C. Li, Z. Zhou, and M. Liu, Enhancing the spin-orbit torque efficiency by the insertion of a sub-nanometer beta-W layer, ACS Nano **16,** 11852 (2022).

[33] Q. Lu, Y. Li, B. Peng, H. Tang, Y. Zhang, Z. He, L. Wang, C. Li, W. Su, Q. Yang, Z. Zhou, and M. Liu, Enhancement of the spin-mixing conductance in CoFeB/W bilayers by interface engineering, Phys. Rev. Appl. **12,** 064035 (2019).

[34] M. Hayashi, J. Kim, M. Yamanouchi, and H. Ohno, Quantitative characterization of the spin-orbit torque using harmonic Hall voltage measurements, Phys. Rev. B **89,** 144425 (2014).

[35] D. Zhu, Y. Wang, S. Shi, K.-L. Teo, Y. Wu, and H. Yang, Highly efficient charge-to-spin conversion from in situ Bi_2Se_3/Fe heterostructures, Appl. Phys. Lett. **118,** 062403 (2021).

[36] P. Deorani and H. Yang, Role of spin mixing conductance in spin pumping: Enhancement of spin pumping efficiency in Ta/Cu/Py structures, Appl. Phys. Lett. **103,** 232408 (2013).

[37] L. Zhu, L. Zhu, D. C. Ralph, and R. A. Buhrman, Origin of strong two-magnon scattering in heavy-metal/ferromagnet/oxide heterostructures, Phys. Rev. Appl. **13,** 034038 (2020).

[38] Y. Liu, Z. Yuan, R. J. Wessenlink, A. A. Starikov, and J. P. Kelly, Interface enhancement of Gilbert damping from first principles, Phys. Rev. Lett. **113,** 207202 (2014).

[39] Q. Hao and G. Xiao, Giant spin Hall effect and switching induced by spin-transfer torque in a $W/Co_{40}Fe_{40}B_{20}/MgO$ structure with perpendicular magnetic anisotropy, Phys. Rev. Appl. **3,** 034009 (2015).

[40] J. Bass and W. P. J. Pratt, Spin-diffusion lengths in metals and alloys, and spin-flipping at metal/metal interfaces: An experimentalist's critical review, J. Phys.: Condens. Matter **19,** 183201 (2007).

[41] Y. Wang, R. Ramaswamy, and H. Yang, FMR-related phenomena in spintronic devices, J. Phys. D: Appl. Phys. **51,** 28 (2018).

[42] Y. Wang, R. Ramaswamy, M. Motapothula, K. Narayanapillai, D. Zhu, J. Yu, T. Venkatesan, and H. Yang, Room-temperature giant charge-to-spin conversion at the $SrTiO_3$-$LaAlO_3$ oxide interface, Nano Lett. **17,** 7659 (2017).

[43] H. Yang, B. Zhang, X. Zhang, X. Yan, W. Cai, Y. Zhao, J. Sun, K. L. Wang, D. Zhu, and W. Zhao, Giant charge-to-spin conversion efficiency in $SrTiO_3$-based electron gas interface, Phys. Rev. Appl. **12,** 034004 (2019).

[44] Y. Li, F. Zeng, S. S. Zhang, H. Shin, H. Saglam, V. Karakas, O. Ozatay, J. E. Pearson, O. G. Heinonen, Y. Wu, A. Hoffmann, and W. Zhang, Giant anisotropy of Gilbert damping in epitaxial CoFe films, Phys. Rev. Lett. **122,** 117203 (2019).

[45] R. Itoh, Y. Takeuchi, S. DuttaGupta, S. Fukami, and H. Ohno, Stack structure and temperature dependence of spin-orbit torques in heterostructures with antiferromagnetic PtMn, Appl. Phys. Lett. **115,** 242404 (2019).

[46] Y.-C. Lau and M. Hayashi, Spin torque efficiency of Ta, W, and Pt in metallic bilayers evaluated by harmonic Hall and spin Hall magnetoresistance measurements, Jpn. J. Appl. Phys. **56,** 0802B0805 (2017).

[47] G. Shi, E. Liu, Q. Yang, Y. Liu, K. Cai, and H. Yang, Composition dependence of spin–orbit torques in PtRh/ferromagnet heterostructures, APL Mater. **9,** 041105 (2021).

[48] Y. Ou, S. Shi, D. C. Ralph, and R. A. Buhrman, Strong spin Hall effect in the antiferromagnet PtMn, Phys. Rev. B **93,** 220405(R) (2016).

[49] W. Zhang, W. Han, X. Jiang, S.-H. Yang, and S. S. P. Parkin, Role of transparency of platinum–ferromagnet interfaces in determining the intrinsic magnitude of the spin Hall effect, Nat. Phys. **11**, 496 (2015).

[50] N. Nakajima, T. Koide, T. Shidara, H. Miyauchi, H. Fukutani, A. Fujimori, K. Iio, T. Katayama, M. Nývlt, and Y. Suzuki, Perpendicular magnetic anisotropy caused by interfacial hybridization via enhanced orbital moment in Co/Pt multilayers: Magnetic circular x-ray dichroism study, Phys. Rev. Lett. **81**, 5229 (1998).

[51] M. Suzuki, H. Muraoka, Y. Inaba, H. Miyagawa, N. Kawamura, T. Shimatsu, H. Maruyama, N. Ishimatsu, Y. Isohama, and Y. Sonobe, Depth profile of spin and orbital magnetic moments in a subnanometer Pt film on Co, Phys. Rev. B **72**, 054430 (2005).

[52] R. Hao, K. Zhang, Y. Li, Q. Cao, X. Zhang, D. Zhu, and W. Zhao, Probing the magnetization switching with in-plane magnetic anisotropy through field-modified magnetoresistance measurement, Chin. Phys. B **31**, 017502 (2022).

[53] Y.-T. Liu, T.-Y. Chen, T.-H. Lo, T.-Y. Tsai, S.-Y. Yang, Y.-J. Chang, J.-H. Wei, and C.-F. Pai, Determination of spin-orbit-torque efficiencies in heterostructures with in-plane magnetic anisotropy, Phys. Rev. Appl. **13**, 044032 (2020).

[54] D. Zhao, Y. Wang, J. Shao, Y. Chen, Z. Fu, Q. Xia, S. Wang, X. Li, G. Dong, M. Zhou, and D. Zhu, Temperature dependence of tunnel magnetoresistance in serial magnetic tunnel junctions, AIP Adv. **12**, 055114 (2022).